Earth and Planetary Science Letters 565 (2021) 116935

Contents lists available at ScienceDirect

Earth and Planetary Science Letters

www.elsevier.com/locate/epsl

Expanded lacustrine sedimentation in the Qaidam Basin on the northern Tibetan Plateau: Manifestation of climatic wetting during the Oligocene icehouse

Minghao Wu [a], GuangSheng Zhuang [a,*], Mingqiu Hou [a], Zhonghui Liu [b]

[a] Department of Geology and Geophysics, Louisiana State University, Baton Rouge, LA 70810, USA
[b] Department of Earth Sciences, The University of Hong Kong, Hong Kong, China

ARTICLE INFO

Article history:
Received 17 September 2020
Received in revised form 27 March 2021
Accepted 4 April 2021
Available online xxxx
Editor: R. Bendick

Keywords:
Inner Asia
westerlies
East Asian summer monsoon
compound specific hydrogen isotope
Qaidam Basin

ABSTRACT

The Qaidam Basin in the core area of arid Inner Asia has been considered undergoing continuous aridification over the Cenozoic. However, the Qaidam Basin is marked with expanded lacustrine sedimentation during the Oligocene, which contrasts with the fluvial or deltaic facies stratigraphically below (Eocene) and above (Miocene-present). The Oligocene lacustrine expansion challenges the idea of persistent aridification. To solve the conundrum, we reconstruct a long-term compound-specific hydrogen isotope (δ^2H) record from sedimentary leaf wax *n*-alkanes to evaluate the paleoclimatic context before, during, and after the Oligocene lacustrine expansion. The δ^2H results reveal three shifts at ca. 40 Ma, 34 Ma, and 24 Ma. The leaf wax δ^2H values range from −176.8‰ to −166.7‰ from 51 to 40 Ma, followed by an abrupt increase of 23.9‰ at 40 Ma. We interpret this rapid increase as enhanced aridification due to the coeval retreat of the Paratethys Sea from the region. At 34 Ma, the δ^2H plunges across the Eocene-Oligocene transition (EOT). Post-EOT δ^2H values are the lowest, vary with high amplitude from −187.1‰ to −153.2‰, and are associated with the lacustrine facies expansion, indicating a wetter climate. By compiling the regional isotopic proxy studies, we observe the contrasting patterns in paleohydrology conditions since the EOT: the relaxation of aridity in the westerlies region versus the enhanced aridification in the East Asian summer monsoon region. We interpret that the west-east contrasting patterns represent the different climatic responses to global cooling: wetting in the west as a result of the enhanced moisture transport via westerlies replacing the subtropical high, and drying in the east due to the reduction in moisture content associated with weakening East Asian summer monsoon. Wetting in Inner Asia is synchronous with cooling in the ocean (North Atlantic) and on land (Xining Basin). Since 24 Ma, δ^2H increases in response to warming during the latest Oligocene to the early Miocene when the subtropical high re-occupied Inner Asia, causing the aridity. This study reveals a dynamic climate in Inner Asia with different mechanisms responding to global change.

1. Introduction

The Qaidam Basin is a huge intermontane basin (150 to 300 km wide and 800 km long) in the core area of Inner Asia. The Cenozoic sedimentary sequence in the Qaidam Basin is marked with the basin-wide lacustrine facies in the Oligocene, which contrasts to other Cenozoic periods that are dominated by the fluvial, deltaic, or alluvial fan facies (Wang et al., 2007; Yin et al., 2002; Zhuang et al., 2011). The expansion of paleo-lake in the Qaidam Basin is unexpected in the context of persistently arid Inner Asia. A modern-like climate pattern with extreme aridity in Inner Asia was suggested to have been present since the early Eocene (Caves et al., 2015). Many mechanisms have been proposed to explain the arid climate in Inner Asia, which includes the control on climate by subtropical high and the enhanced aridity associated with the uplift of Tibetan Plateau, the retreat of Paratethys Sea, and global cooling. The control of subtropical high, causing the arid climate in a wide region extending from Inner Asia to the east coast of China in the Paleogene, is founded on the records of xerophytic pollens and evaporation minerals (Guo et al., 2008). Climate modeling results show that the uplift of the Tibetan Plateau blocks moistures and leads to unevenly distributed latent heating of the atmosphere, which produces high-pressure zones with subsiding dry air in Inner Asia (e.g., Broccoli and Manabe, 1992). The climatic effect of the uplift of the Tibetan Plateau is supported by

* Corresponding author.
E-mail address: gzhuang@lsu.edu (G. Zhuang).

https://doi.org/10.1016/j.epsl.2021.116935
0012-821X/

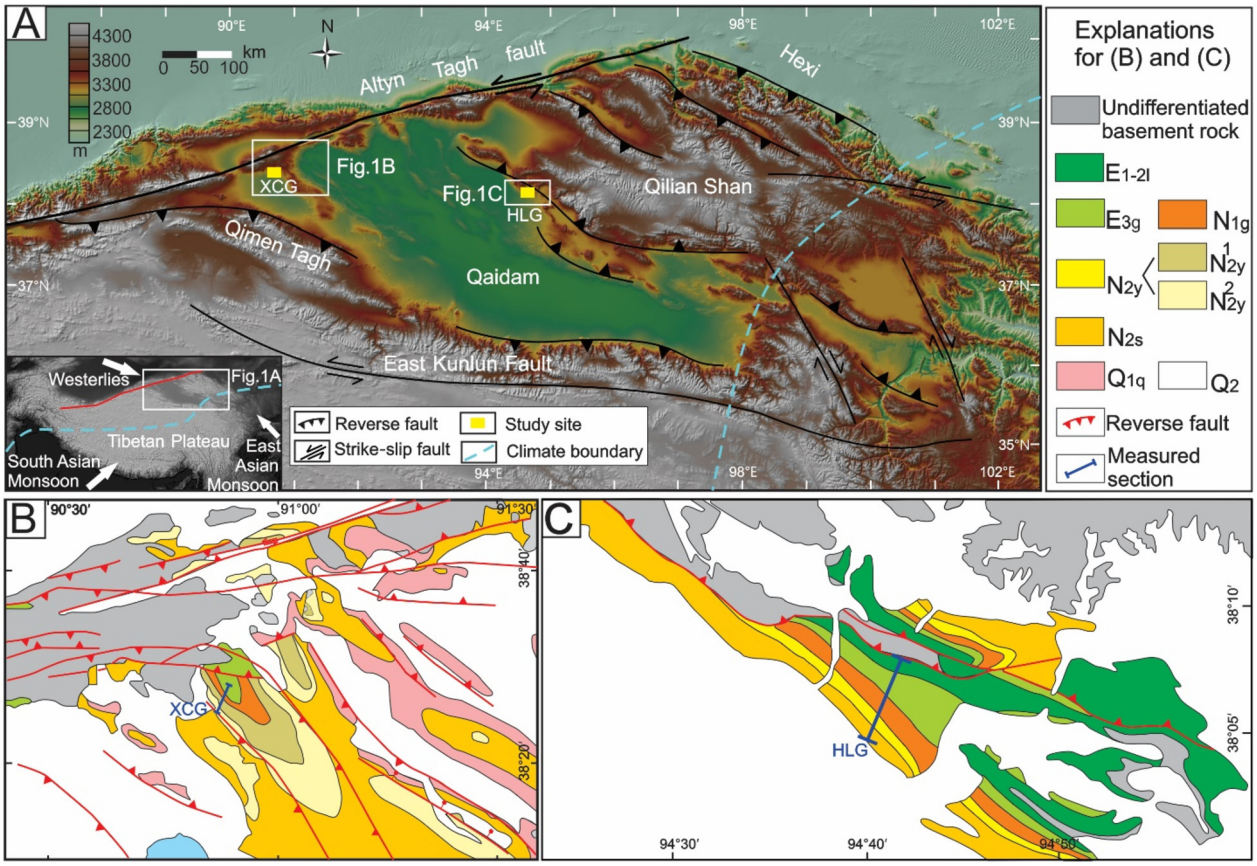

Fig. 1. A: Topography and geology of the northern Tibetan Plateau with superimposed color representing elevation. The inset shows the Tibetan Plateau. The red line in the inset denotes the Altyn Tagh fault. The blue dashed line denotes the climate boundary that separates the westerlies-dominating region to the west and the Asian summer monsoon-controlling region to the east. B: Simplified geological map of the western Qaidam Basin (modified from Chang et al., 2015). C: Simplified geological map of the northwestern Qaidam Basin (modified from Li et al., 2020 and Zhang, 2006). Legend: $E_{1\text{-}2l}$, Lulehe Formation (early Eocene); E_{3g}, Xia Ganchaigou Formation (middle-late Eocene); N_{1g}, Shang Ganchaigou Formation (Oligocene); N_{2y}, Youshashan Formation including N^1_{2y}, Xia Youshashan Formation (early-middle Miocene) and N^2_{2y}, Shang Youshashan Formation (middle-late Miocene); N_{2s}, Shizigou Formation (late Miocene-Pliocene); Q_{1q}, Qigequan Formation (Pliocene-Pleistocene); Q_2, late Pleistocene and Holocene. The abbreviations of studied sections: HLG, Hongliugou section; XCG, Xichagou section. (For interpretation of the colors in the figure(s), the reader is referred to the web version of this article.)

fluvial-lacustrine carbonate $\delta^{18}O$ studies that support the Eocene uplift of Tibetan Plateau and blocking moisture and isolating basins (Graham et al., 2005; Kent-Corson et al., 2009). The retreat of the Paratethys Sea – an epicontinental sea extending from northwest China to the Mediterranean – would reduce the moisture transport from the west (Bosboom et al., 2014a; Zhang et al., 2007). Global cooling since the early Eocene, especially at the Eocene-Oligocene transition (EOT), contributes to the aridification in Inner Asia by reducing the atmospheric moisture content and weakening East Asia summer monsoon (Dupont-Nivet et al., 2007; Licht et al., 2014).

None of the above mechanisms can explain the expansion of lacustrine sedimentation in the Qaidam Basin. The discrepancy between expanded lacustrine facies and persistent aridity is further complicated by a fossil leaf study that suggests a wetter climate in the Qaidam Basin at ca. 31 Ma (Song et al., 2020). The paleo-lake evolution could be a result of local geology (Carroll and Bohacs, 1999). Adding to the complexity is the lack of evaluation on the relationship between the expanded lacustrine sedimentation and the kinematic history of the left-lateral, strike-slip Altyn Tagh fault that bounds the Qaidam Basin to the northwest (Fig. 1A).

To resolve the discrepancy between the paleo-lake expansion and the proposed arid climate and to offer a paleohydrological basis to evaluate the role of tectonism, we design a holistic research project with three goals. (1) We first reconstruct a long-term climatic history to evaluate the paleohydrological condition before, during, and after the paleo-lake expansion. We apply the compound-specific hydrogen isotope analysis (δ^2H) (see a review in Sachse et al., 2012) to sedimentary leaf wax *n*-alkanes. We study two sedimentary sections in the Qaidam Basin on the northern Tibetan Plateau to illuminate the systematic climate pattern across the basin (Fig. 1). (2) We then reconstruct the regional climatic regime by compiling and contrasting available paleohydrological proxy studies. (3) In the established paleohydrological context, we propose a new mechanism that synthesizes geological observations and is compatible with climatic modeling studies.

2. Geological setting

The Qaidam Basin is an intermontane basin located on the northern Tibetan Plateau. It covers 120,000 km^2 and lies at a mean elevation of 2800 m. The basin is bounded by the left-lateral strike-slip Altyn Tagh fault to the northwest, the Qilian Shan thrust belt to the northeast, and the Qimen Tagh-Eastern Kunlun thrust belt to the south (Fig. 1A).

The Cenozoic Qaidam Basin is filled with terrestrial sediments of ca. 12,000 m in the basin center. The Cenozoic sedimentary sequence is divided into seven lithostratigraphic units: the Lulehe (LLH) Formation (early Eocene), the Xia Ganchaigou (XGCG) Formation (middle-late Eocene), the Shang Ganchaigou (SGCG) Formation (Oligocene), the Xia Youshashan (XYSS) Formation (early-

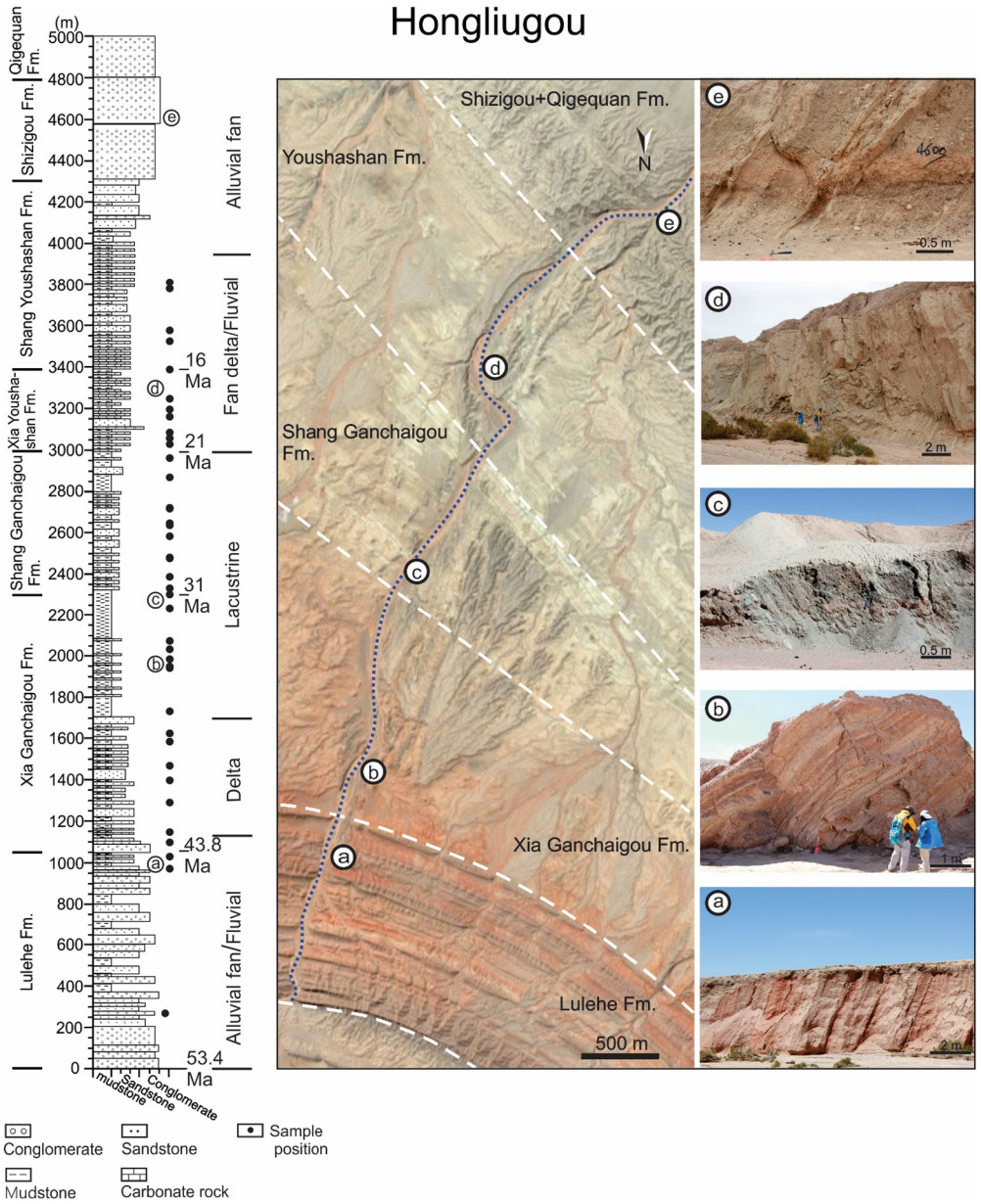

Fig. 2. Sedimentary sequence, satellite image (from Google Earth, https://www.google.com/earth/), and representative lithology at the Hongliugou (HLG) section. The blue dashed line on the satellite image shows the studied Hongliugou section. Representative lithology: (a) the interbedded mudstone (red color) and medium-coarse sandstone (light color) of fluvial deposits; (b) the interbedded mudstone (red color) and siltstone (light color) of marginal lacustrine or deltaic deposits; (c) the green mudstone of lacustrine deposits; (d) the yellow-brown sandstone of fluvial or fan delta deposits; (e) the yellow-brown conglomerate of alluvial fan deposits. (For interpretation of the colors in the figure(s), the reader is referred to the web version of this article.)

middle Miocene), the Shang Youshashan (SYSS) Formation (middle-late Miocene), the Shizigou (SZG) Formation (late Miocene to Pliocene), and the Qigequan (QGQ) Formation (Pliocene to Pleistocene) (Chang et al., 2015; Fang et al., 2007; Sun et al., 2005; Yin et al., 2008).

The climate of the present Qaidam Basin is arid. The mean annual precipitation (MAP) varies from less than 100 mm in the northwest to 150-200 mm in the eastern Qaidam Basin; the basin center is much drier with MAP of about 50 mm (Du and Sun, 1990). Atmospheric moistures are mainly transported by the westerlies to the western Qaidam Basin and by the East Asian summer monsoon (EASM) to the east (Fig. 1) (Chen et al., 2019).

We studied two sections in the Qaidam Basin: the Hongliugou (HLG) (from 38°08.107′N, 94°41.279′E to 38°05.368′N, 94°39.645′E) and the Xichagou (XCG) (from 38°25.835′N, 90°53.363′E to 38°22.762′N, 90°52.411′E) (Fig. 1A). The thickness of the Hongliugou and Xichagou is ca. 5000 m and ca. 4500 m, respectively.

The Hongliugou section consists of all the Cenozoic formations from the Lulehe Formation (early Eocene) at the bottom to the Qigequan Formation (Pliocene to Pleistocene) on the top (Fig. 2). The Lulehe (LLH) Formation is dominated by the alluvial fan and fluvial facies. The Xia Ganchaigou Formation consists of deltaic facies at the lower portion and lacustrine facies at the upper portion. The Shang Ganchaigou Formation mainly consists of lacustrine facies. The Xia Youshashan Formation and the Shang Youshashan Formation are dominated by fan delta and fluvial facies. The Shizigou Formation and the Qigequan Formation are dominated by alluvial fan facies. The detailed lithology and sedimentary facies of the Hongliugou section have been described in Zhuang et al. (2011).

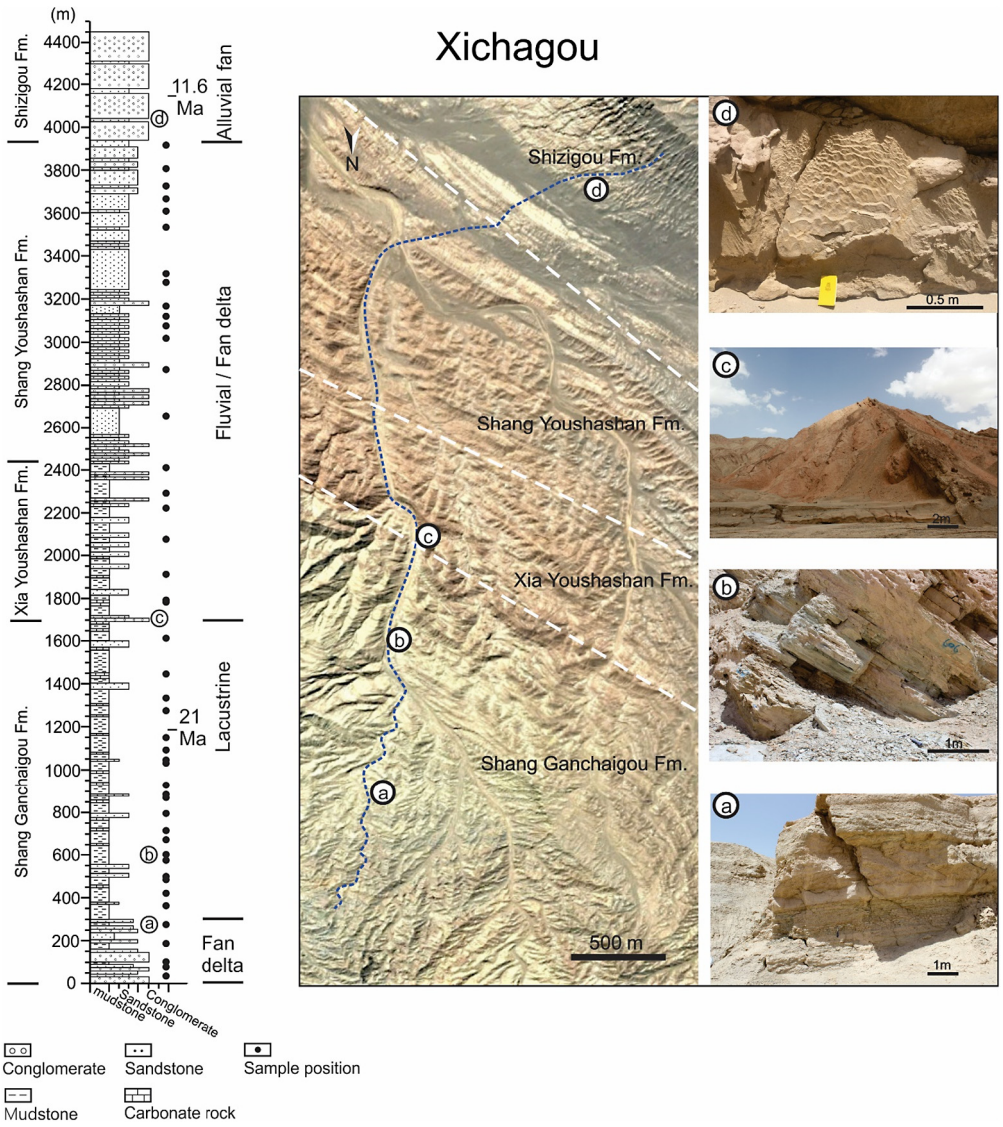

Fig. 3. Sedimentary sequence, satellite image (from Google Earth, https://www.google.com/earth/), and representative lithology of the Xichagou (XCG) section. The blue dashed line on the satellite image shows the studied Xichagou section. Representative lithology: (a) the green laminated mudstone of lacustrine deposits overlaid by the light brown conglomerate of fan delta; (b) green laminated mudstone of lacustrine deposits; (c) the red-brown conglomerate of fan delta deposits; (d) the light brown coarse sandstone with asymmetrical ripples of fluvial or alluvial fan deposit. (For interpretation of the colors in the figure(s), the reader is referred to the web version of this article.)

The Xichagou section in the western Qaidam Basin consists of sedimentary strata from the Shang Ganchaigou Formation (Oligocene) to Shizigou Formation (Miocene). The Shang Ganchaigou Formation is dominated by lacustrine facies. Above the Shang Ganchaigou Formation, the Xia Youshashan Formation and the Shang Youshashan Formation are dominated by fluvial facies and fan delta facies. The Shizigou Formation is dominated by alluvial fan facies (Fig. 3). The detailed lithology and sedimentary facies of the Xichagou section have been described in Zhuang et al. (2011).

The ages of the Hongliugou and Xichagou sections have been dated via magnetostratigraphy and biostratigraphy (Chang et al., 2015; Wang et al., 2007; Zhang, 2006). The age of the Hongliugou section has been constrained to 53.4 to 2.4 Ma (Zhang, 2006). The complete magnetostratigraphy result of the Hongliugou section has been published in Li et al. (2020). The early Eocene age of the Lulehe Formation at the Hongliugou section is consistent with a previous magnetostratigraphy study in the northwest Qaidam Basin (Sun et al., 2005). Based on ostracod assemblages, Sun et al. (2005) assigned a late Eocene age for the top of Xia Ganchaigou Formation, implying that the age of the underlying Lulehe Formation is older than late Eocene. Two younger age models (ca. 25 and 21 Ma) for the Lulehe Formation have been proposed in the Dahonggou area in the northeastern Qaidam Basin (Nie et al., 2019; Wang et al., 2017). The difference in age for the Lulehe Formation between the eastern and western Qaidam Basin may indicate the diachroneity in sedimentation across the basin (Cheng et al., 2018). The 53.4 Ma age model is used here, given that the in-situ magnetostratigraphic study was conducted in the Hongliugou section and is supported by lithostratigraphic correlation to the western and northwestern parts that have independent age constraints.

In the Xichagou region, the strata have been dated to 30 to 10 Ma (Chang et al., 2015; Zhang, 2006). Chang et al. (2015) proposed two possible magnetostratigraphic correlations for the bottom of the Huatugou section (within hundreds of meters away from the Xichagou section): one correlation suggests ca. 28 Ma, and the other suggests ca. 31 Ma. The later age model accords with the magnetostratigraphy study in the Xichagou section, which designates the bottom age as ca. 31 Ma (Zhang, 2006). Hence, we adopt ca. 31 Ma as the bottom age of the Xichagou section.

3. Method

3.1. Sample collection

We have collected 90 fine-grained (mudstone and siltstone) samples, 44 samples from the Hongliugou section and 46 samples from the Xichagou section. The loose weathered surface was removed in the field. The sample ages are determined through the linear interpolation between the ages of major magnetostratigraphic chrons (Table S1).

3.2. Organic matter extraction

Before extraction, samples were crushed into granule size, freeze-dried for 48 hours, and stored in the fridge. Total lipids were extracted from the preprocessed samples (ca. 150 to 750 g) by using the Soxhlet extractors with 2:1 (v/v) of dichloromethane (DCM)/methanol (MeOH) for 48 hours. The total lipid extracts (TLE) were then concentrated using Biotage TurboVap Classic II under purified nitrogen stream at 40 °C in the water bath. The total lipid extracts were eluted sequentially with 4 ml hexane, 4 ml dichloromethane, and 4 ml methanol through glass pipettes filled with activated silica gel (ca. 4.0 g) and separated into aliphatic, aromatic, and polar fractions. The aliphatic fraction containing *n*-alkanes was further purified by urea adduction to remove the branched and cyclic alkanes.

3.3. Carbon preference index

The distribution of *n*-alkanes was determined by using a Thermo Trace 1310 Gas Chromatography-Flame ionization detector (GC-FID) equipped with a Thermo Scientific TG-1MS column (60 m long, 0.25 mm i.d., 0.25 um film thickness). The *n*-alkanes are carried by helium with a flow rate of 2 ml/min. The GC temperature was programmed to ramp from 60 °C (held for 1 min) to 320 °C at 15 °C/min with an isothermal holding for 20 minutes. The peak areas of *n*-alkanes calculated through Xcalber software correspond to the relative abundances of *n*-alkanes.

The carbon preference index (CPI) was calculated by the following equation:

$$\mathrm{CPI} = 0.5 \times \Sigma A(23\text{-}33)/\Sigma A(24\text{-}34) + 0.5 \times \Sigma A(25\text{-}35)/\Sigma A(24\text{-}34) \quad (1)$$

where A is the area of the individual *n*-alkane peak; 23-33, 24-34, and 25-35 represent odd and even number *n*-alkanes.

3.4. Isotope analysis

The hydrogen isotope composition (δ^2H) of *n*-alkanes were measured using a Trace Gas Chromatography (GC) 1310 coupled to a Thermo Delta V Advantage Isotope Ratio Mass Spectrometer (IRMS) with a Thermo Isolink interface. A Thermo Scientific TG-5MS column (30 m long, 0.25 mm i.d., 0.25 um film thickness) was used. The *n*-alkanes were pyrolyzed to hydrogen gas in a High-Temperature Converter (HTC) reactor at 1400 °C and then transported to IRMS. The H^{3+} factor was measured daily at the beginning of each analysis sequence. The average value of the H^{3+} factor is 5.32 ppm mV^{-1} ($\pm$0.17, $n = 43$) during the period of hydrogen isotope analysis. The GC carrier gas is helium with a flow rate of 2 ml/min. The GC temperature was programmed to ramp from 60 °C (with an isothermal holding) for 2 min to 170 °C at 14 °C/min, then to 300 °C at 3 °C/min, and finally to 320 °C at 14 °C/min followed by an isothermal holding for 5 minutes.

The δ^2H values are corrected against the reference material (Mix A6, A. Schimmelmann, Indiana University Bloomington) and reported against Vienna Standard Mean Ocean Water (VSMOW). The δ^2H values for *n*-alkanes nC$_{16}$-nC$_{30}$ of Mix A6 are −9.1‰, −117.8‰, −52.0‰, −56.3‰, −89.7‰, −177.8‰, −81.3‰, −67.2‰, −29.7‰, −263.0‰, −45.9‰, −172.8‰, −36.8‰, −177.8‰, and −213.6‰. Mix A6 was measured every six sample analyses. All samples are analyzed with at least one replicate (Table S1). For the reported δ^2H values, the minimum peak intensity of 1000 mV was required. The δ^2H values are reported using the following equation:

$$\delta^2\mathrm{H} = (R_{\mathrm{sample}}/R_{\mathrm{standard}} - 1) \times 1000 \quad (2)$$

where $R = {}^2\mathrm{H}/{}^1\mathrm{H}$. δ^2H values are expressed in per mil (‰).

4. Results

The carbon preference index (CPI) values vary between 7.5 and 1.0 (Table S1). Samples with high CPI ($\geq$2.0) values are represented by the filled circles in Fig. 4A, and the samples with low CPI (1.0 to 2.0) are represented by the empty circles. For samples with low CPI values, a large amount of sample (up to ca. 750 g) has been extracted to obtain enough *n*-alkanes for δ^2H analysis (see Section 3.2). There is no systematic trend for samples with low CPI values (Fig. 4A).

The nC$_{29}$ and nC$_{31}$ (*n*-alkanes with 29 and 31 carbon atoms) are the most abundant homologs of long-chain *n*-alkanes, and their δ^2H values show a good correlation with the coefficients of 0.84 in the Hongliugou and 0.77 in the Xichagou (Fig. S1). We focus discussions on the δ^2H of nC$_{29}$ from the Hongliugou and Xichagou sections in this paper (Table S1; Fig. 4A).

For the Hongliugou section, the δ^2H values are relatively stable during the interval of 51 to 40 Ma and vary from −176.8‰ to −166.7‰. An abrupt increase of 23.9‰ occurs at 40 Ma. δ^2H values are high from 40 to 35 Ma and vary between −165.4‰ and −142.9‰. The Hongliugou section is marked by very low δ^2H values between 34 and 24 Ma. The δ^2H decreases by 27‰ from −142.9‰ to −169.5‰ at ca. 34 Ma. The low values with a large amplitude of variation from −187.1‰ to −153.2‰ retain until ca. 24 Ma when the δ^2H increases from −182.9‰ to −161.7‰. From ca. 21 to 12 Ma, the δ^2H values are high and vary between −169.0‰ and −140.1‰.

The δ^2H values from the Xichagou section overlap with the Hongliugou section, varying from −187.6‰ to −143.8‰. In detail, the δ^2H values are generally low from ca. 30 to 24 Ma, varying with large amplitude from −151.3‰ to −178.2‰. From ca. 24 to 12 Ma, the δ^2H values are slightly higher than the previous interval and vary between ca. −174.0‰ and ca. −150.0‰.

5. Discussions

5.1. Eocene aridification of Inner Asia

The Hongliugou section obtains the oldest record of leaf wax *n*-alkane δ^2H. The δ^2H values from the Hongliugou section are relatively stable during the interval of 51 to 41 Ma with moderate isotopic values for the whole sequence (Fig. 4A). At ca. 41 Ma, the leaf wax δ^2H values increase sharply by 23.9‰ (Fig. 4A). The increase in δ^2H is synchronous with the enhanced aridification in the Xining Basin to the east of our study area (Bosboom et al., 2014b; Meijer et al., 2019). In the Xining Basin, the saline lake shrank at ca. 41 Ma; thick gypsum layers, which was interpreted to indicate a saline lake in the less arid environment, were replaced by thin gypsum intercalations with arid mudflat deposits (Meijer et

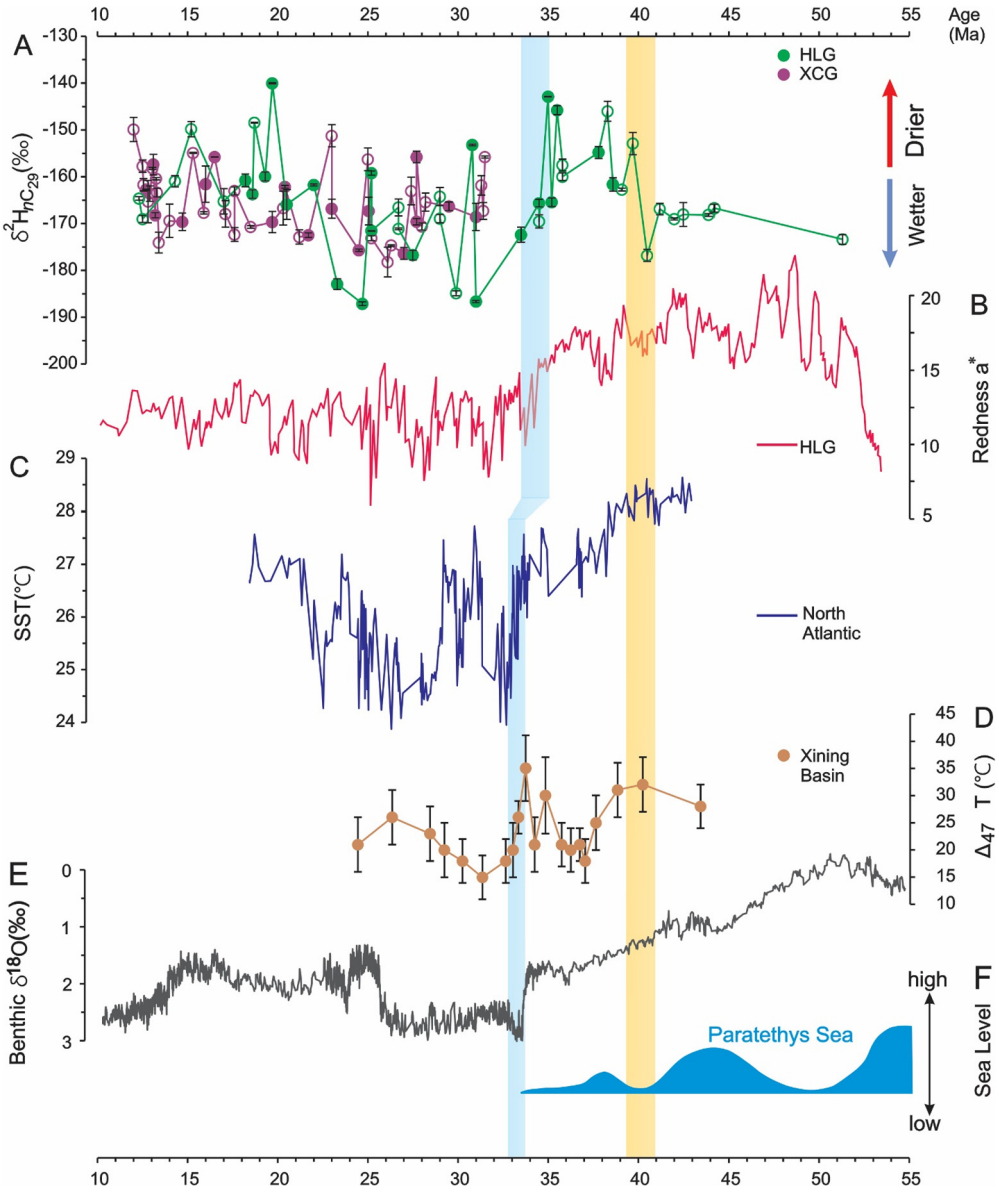

Fig. 4. A: Leaf wax δ^2H for *n*-alkane nC_{29} from Hongliugou (HLG) and Xichagou (XCG) sections. The bars represent $\pm$ 1σ standard error. The empty circles indicate samples with low CPI (1.0 to 2.0) values. The filled circles indicate samples with high CPI ($\geq$2.0) values. B: Redness of the HLG section (Han, 2008). C: North Atlantic sea surface temperatures (SST) (Liu et al., 2018). D: Carbonate clumped isotope (Δ_{47})-based temperature reconstructions in the Xining Basin (bars for 1σ standard errors) (Page et al., 2019). E: Global benthic foram δ^{18}O (Zachos et al., 2001). F: Sea level of the Paratethys Sea (Bosboom et al., 2014a). The blue color highlights the Eocene-Oligocene transition. The yellow color denotes the retreat of Paratethys Sea from the Tarim Basin. (For interpretation of the colors in the figure(s), the reader is referred to the web version of this article.)

al., 2019). Also, pollen records in the Xining Basin show an increase in steppe-desert taxa and a decrease in broad-leaved trees, indicating a drier climate (Bosboom et al., 2014b).

The observation of enhanced aridity in the Xining Basin at ca. 41 Ma has been linked to the regional drying in Inner Asia due to the retreat of the Paratethys Sea. The Paratethys Sea occupied a large area spanning from Europe to the Tarim Basin in Inner Asia during Paleogene (Bosboom et al., 2014a). Three Cenozoic sea-level cycles were identified from 65 to 48 Ma, 48 to 41 Ma, and 41 to 35 Ma, respectively (Fig. 4D) (Bosboom et al., 2014a; Meijer et al., 2019): (1) the first and second transgressions extended throughout the southwest part of Tarim Basin; (2) the third transgression is the smallest and only reached Tarim Basin's western margin (Bosboom et al., 2014a). These observations revealed the westward retreat of the Paratethys Sea, which is supported by the transition from marine strata to terrestrial strata in the western Tarim Basin at ca. 41 Ma (Bosboom et al., 2014a).

Given the synchroneity, we interpret that the abrupt increase in leaf wax *n*-alkane δ^2H values at 41 Ma document the aridification in the Qaidam Basin due to the retreat of the Paratethys Sea, which caused the loss of a major moisture source for Inner Asia. The causal relationship between the aridification in Inner Asia and the retreat of Paratethys Sea has been established by numerical modeling, which reveals that the retreat of Paratethys Sea from the Tarim Basin caused the reduction in the annual precipitation in Inner Asia by ca. 20% (Zhang et al., 2007). There are several reasons which explain that the aridification imprints on the leaf wax *n*-alkane hydrogen isotopes (δ^2H). In an arid climate, low humidity enhances the sub-cloud evaporation, which enriches heavy hydrogen isotopes in precipitation (Li and Garzione, 2017) – the source water of leaf wax *n*-alkane hydrogen isotopes (Sachse et al., 2012). The loss of nearby moistures also increases the relative contribution of recycling moistures, which are derived from local surface water bodies, including lake and river waters with high δ^2H values

(Li and Garzione, 2017). Additionally, low humidity enhances leaf transpiration, which enriches heavy hydrogen isotopes in leaf water that is used in the biochemical synthesis of *n*-alkanes (Sachse et al., 2012).

The increase in δ^2H values is not driven by temperature variations. The global temperature decreases since the early Eocene (Fig. 4E) (Zachos et al., 2001). The temperature effect will impart low δ^{18}O values to precipitations under low temperatures and low δ^2H values given that δ^{18}O correlates with δ^2H on the global/local meteoric water line (Araguas-Araguas et al., 1996). Hence, the increase in leaf wax *n*-alkane δ^2H that we observe at 41 Ma in the global cooling context means that the aridification effect reverses the temperature effect, which would have caused a decline in leaf wax δ^2H.

Two subsequent sea retreats at ca. 37 and 34 Ma are not documented in the leaf wax δ^2H record (Fig. 4). We argue the lack of signals is due to the following reasons. The magnitudes of these two sea retreats are much smaller than the retreat at ca. 41 Ma (Fig. 4D) (Bosboom et al., 2014a). The impact of sea incursions and retreats after 41 Ma is restricted in Central Asia further to the west of Tarim Basin (Bosboom et al., 2014a). The continental effect will cause the progressive depletion of heavy isotopes in precipitation (Araguas-Araguas et al., 1996), whilst the sea retreat increases the distance between our study area and the moisture source, which amplifies the continental effect. The carbonate clumped isotope (Δ_{47})-based temperatures record a significant temperature drop (>9 °C) in Xining Basin at ca. 38-37 Ma (Page et al., 2019). Along with the global cooling across the EOT at 34 Ma, both will decrease the precipitation δ^2H due to the temperature effect.

5.2. Wetting in the Qaidam Basin during the Oligocene Icehouse

The leaf wax *n*-alkane δ^2H record of the Hongliugou section captures a substantial decrease of 43.7‰ from ca. 35 to 31 Ma. Low δ^2H values are accompanied by large variation (up to ca. 30‰) and continue through the Oligocene epoch (Fig. 4A). The low δ^2H interval overlaps with the interval of expanded lacustrine sedimentation (Fig. 5).

The carbonate clumped isotope (Δ_{47}) study from the Xining basin captures a 20 °C decrease in temperature at the EOT (Page et al., 2019), which is significantly larger than those found in North America (ca. 7 °C) and Europe (ca. 4 to 6 °C) (Fan et al., 2018; Hren et al., 2013) and the sea surface temperature in North Atlantic (Fig. 4). Page et al. (2019) interpret that the large temperature decrease reflects the superimposed effect of regional cooling at EOT and the shift in carbonate precipitation season. We estimate the "temperature effect" on precipitation isotopes with the temperature of 4 to 7 °C, a rate of 0.58‰/°C for δ^{18}O (Araguas-Araguas et al., 1996), and a slope of 8.42 for the δ^{18}O-δ^2H for the local meteoric water line (Li and Garzione, 2017). We derived the equivalent decrease in δ^2H of 19.5 to 34.2‰. The temperature effect cannot fully account for the 43.7‰ decrease in leaf wax δ^2H, indicating a non-thermal signal in the leaf wax hydrogen isotope record.

The comparison between the leaf wax δ^2H and sedimentary redness (Han, 2008) reveals a co-varying pattern (Fig. 4). Across the EOT, the sedimentary redness values decrease sharply from 15 to 10, and low redness values with large fluctuation (up to ca. 5 units) continue through the Oligocene (Han, 2008) (Fig. 4B). The sedimentary redness is determined by the amount of iron oxide minerals (hematite and goethite) (Deaton and Balsam, 1991). Low redness values in the Oligocene correspond to the deeper lacustrine facies with green-grey mudstone and the anoxic environment.

The Oligocene lacustrine facies at the Hongliugou section are punctuated by fluvial and deltaic facies (Fig. 5). The comparison between the δ^2H record and sedimentary facies reveals that the lower δ^2H values correspond to open lacustrine deposits that are characterized by green mudstone or interbedded green and red mudstone (e.g., samples of HLG 32, 34, 36, 39a, and 41), whereas higher δ^2H values during the Oligocene correspond to marginal lacustrine or deltaic deposits characterized by red mudstone or brown siltstone (e.g., samples of HLG 24a, 24b, 33, and 39b) (Fig. 5). The correlation between δ^2H, redness index, and lithology suggest the sedimentary sequence at the Hongliugou section is sensitive to the lake level fluctuations. The spectral analysis on redness data supports the impact of orbital forcing on lake level fluctuations (Han, 2008). We argue that variations in δ^2H with large amplitudes at the Hongliugou section in the Oligocene support the varying climate: lower δ^2H to the wetter climate with higher lake levels and higher δ^2H to relatively drier periods with lower lake levels. The δ^2H records of the Xichagou section from the western Qaidam Basin also show variations with large amplitude from −151.3‰ to −178.2‰ (Fig. 4A), recording the same climatic pattern across this large basin.

Low δ^2H values, anoxic environment, and open lacustrine sedimentation indicate a generally wetter climate in the Qaidam Basin during the Oligocene. Under wetter conditions, the isotopic enrichment effects of evaporation, moisture recycling, and leaf transpiration will be weak (see details in Section 5.1 for the above mechanisms). The inference of wet climate is consistent with the fossil leaf study that found temperate deciduous broad-leaved trees, such as *Populus*, from the 31 Ma strata (Song et al., 2020). Other studies have interpreted the Oligocene strata in the eastern Qaidam Basin as floodplain deposition (e.g., Bush et al., 2016); we emphasize here that the fish fossils were discovered at the Hongliugou section, supporting a lacustrine environment in our study area (e.g., Wang et al., 2007).

In regional geology, Yin et al. (2002) proposed that the basin-bounding Altyn Tagh fault (Fig. 1A) was initiated at early Eocene, and subsequent uplift of Altun Shan along the fault completely closed the outlet of drainages and trapped sediments in the basin at 20 to 10 Ma. Additionally, constraints from piercing points suggest fast slip motion of the Altyn Tagh fault happened during the late Oligocene to early Miocene (Yue et al., 2003). These tectonic events are asynchronous with the lacustrine expansion and wetting climate at ca. 34 Ma. Hence, tectonism may contribute to the formation of internal drainages but is not the direct driver causing the expansion of paleo-lake in the Qaidam Basin.

5.3. Contrasting climatic patterns in Inner Asia and the region to the east

To examine the regional climatic response to the EOT in Inner Asia, we have compiled the regional paleoclimatic proxy studies from a vast region ranging from Tarim Basin in the west to Lanzhou Basin in the east (Fig. 6A). The δ^{18}O of lacustrine and pedogenic carbonates and new leaf wax *n*-alkane δ^2H records from the western Qaidam Basin and Tarim Basin show a decreasing trend across the EOT, synchronous with the expansion of paleolake in the Qaidam Basin, which indicates wetting in the Qaidam Basin. The expansion of lacustrine sedimentation during the Oligocene has also been observed in the basins south and north of the Tian Shan further to the west (Fig. 6A). In contrast, the isotopic records from the eastern Qaidam Basin and the Lanzhou Basin further to the east show an increasing trend since the EOT (Fig. 6B). In the Xining Basin, the desiccation of playa across the EOT (Dupont-Nivet et al., 2007) is linked to the moisture reduction due to global cooling and the resultant aridification and the reduction of inflow from the drainage basins (Dupont-Nivet et al., 2007; Page et al., 2019).

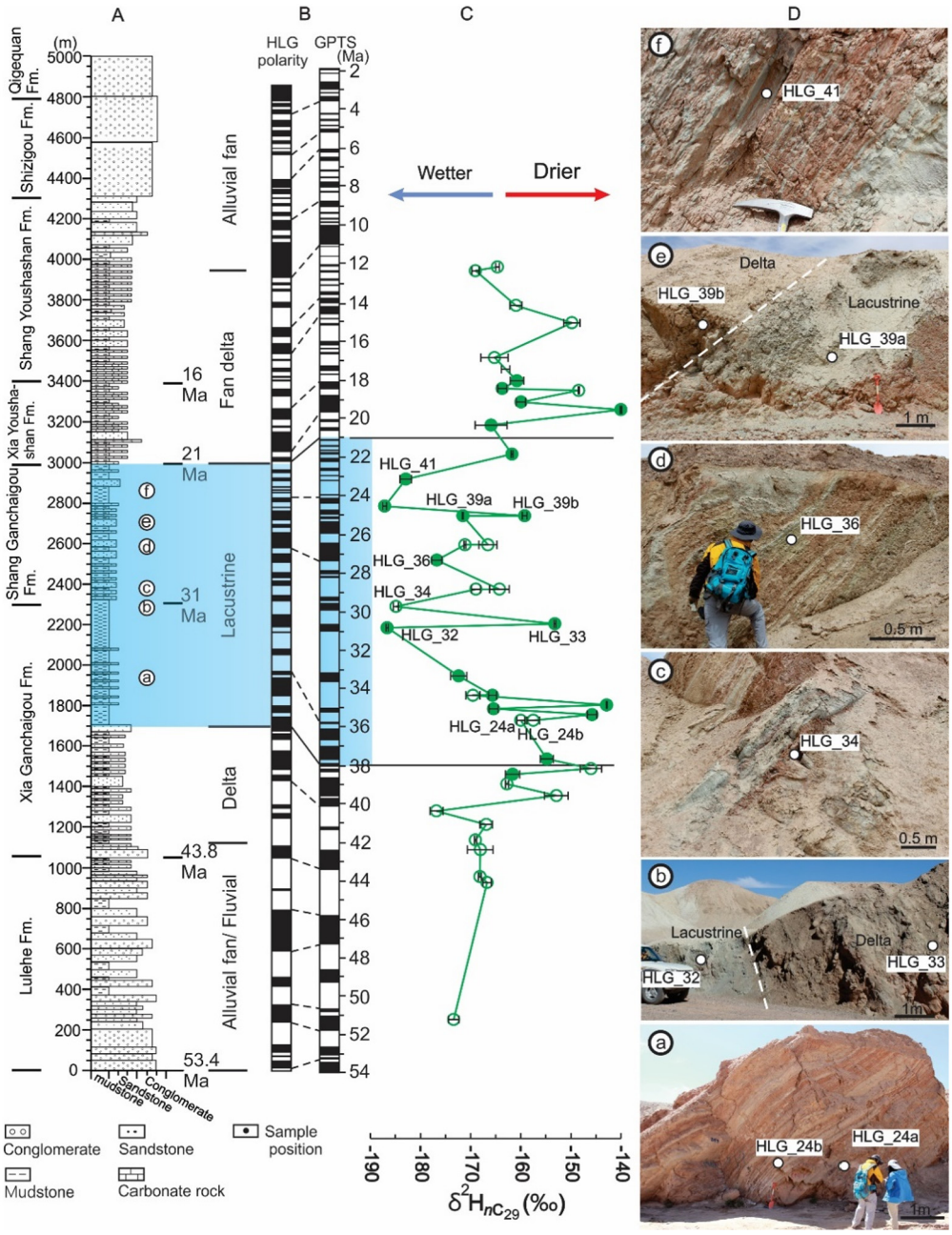

Fig. 5. The lithostratigraphic column of Hongliugou (HLG) section (A); the correlation of observed polarity zones of the Hongliugou section with the geomagnetic polarity time scale (GPTS) (after Li et al., 2020 and Zhang, 2006) (B); δ^2H of leaf wax nC$_{29}$ (C); and representative lithology in the lacustrine interval highlighted by the light blue color across the lithostratigraphic column and geomagnetic polarity time scale (D). (a) the interbedded mudstone (red color) and siltstone (light color) of marginal lacustrine or deltaic deposits, (b) the green mudstone of lacustrine deposits overlaid by brown siltstone and sandstone of deltaic deposits, (c) the interbedded green and red mudstone of lacustrine deposits, (d) the interbedded green and red mudstone of lacustrine deposits, (e) the green mudstone of lacustrine deposits overlaid by brown siltstone and sandstone of deltaic deposits, (f) the interbedded green and red mudstone of lacustrine deposits. The white dots on the field photos show the sampling locations. Refer to Fig. 4A for explanations of symbols in (C). (For interpretation of the colors in the figure(s), the reader is referred to the web version of this article.)

5.4. Mechanisms causing the west-east contrasting climates

The west-east contrasting patterns in isotopic proxies and sedimentary records reflect the diverse climatic responses to global cooling since the EOT: wetting in the west and drying in the east. The East Asian summer monsoon is driven by the thermal difference and atmospheric pressure gradient between the Pacific Ocean and the Asia continent (An, 2000). The Eocene eolian sediments from Xining Basin with the similar grain-size distribution as the typical eolian sediment in East Asia and isotopic studies of fossil tooth and gastropod from Myanmar reveal the monsoonal climate characterized with marked seasonality in wind and precipitation patterns, which support that the Asian Monsoon controlled a vast region from northwest China to Myanmar since the late Eocene (Licht et al., 2014). Monsoonal precipitation in the Xining Basin would decrease by ca. 25% across the EOT due to the decreased continent-ocean pressure gradient and concomitant reduced moisture supply (Licht et al., 2014).

Distinct from the East Asian summer monsoon region, we argue that global cooling manifests its effect in Inner Asia by driving the equatorward migration of westerlies to replace the subtropical high and wetting the region with increasing moistures instead of the subsiding dry air masses. We recognize that the Arctic ice sheet had not developed in the Oligocene (Zachos et al., 2001).

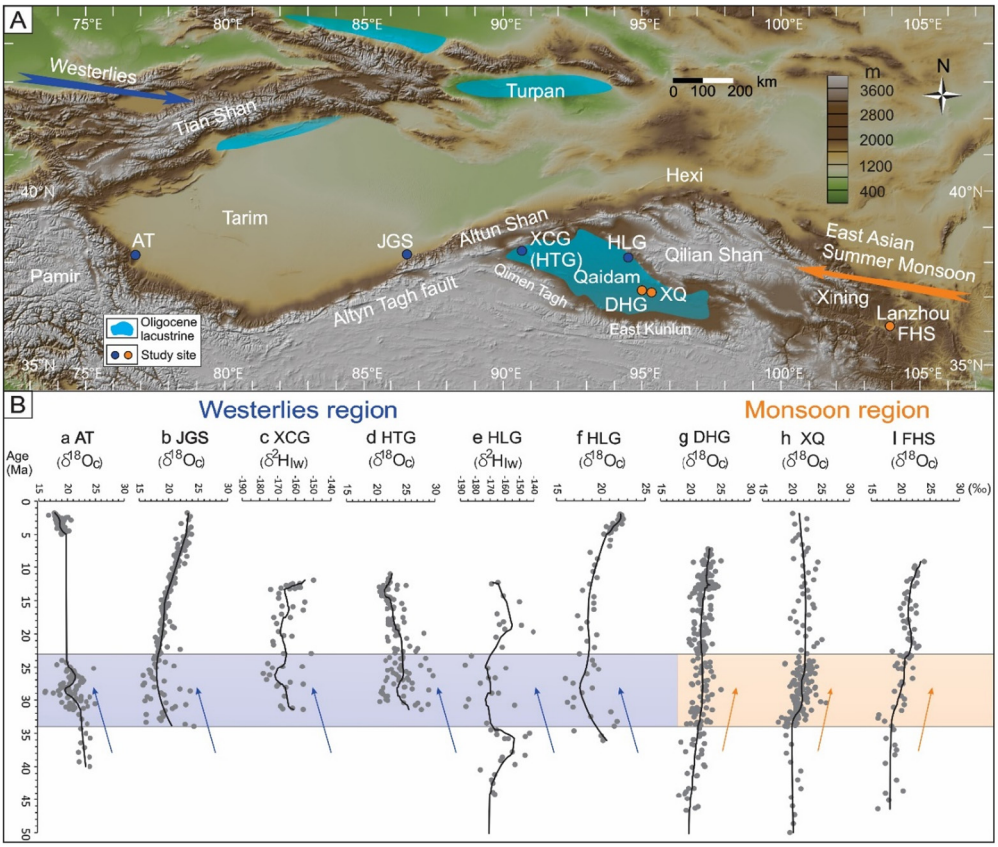

Fig. 6. (A) The topographic map of Inner Asia with the distribution of Oligocene lacustrine deposits (light blue shade) (Lai et al., 2019; Li et al., 2018; Shao et al., 1999; Zhuang et al., 2011) and the localities of paleoclimate studies that are shown in Fig. 6B. Dark blue dots denote study sites with moistures being transported from westerlies; orange dots are the study sites that are influenced by the East Asian summer monsoon. The dark blue color highlights that the local climate became wet in Oligocene, whilst the orange color highlights that the climate became arid. (B) Compilation of paleoclimate data sets. (a) Carbonate $\delta^{18}O$ at the Aertashi section (AT) (Kent-Corson et al., 2009); (b) Carbonate $\delta^{18}O$ at the Janggalsay section (JGS) (Kent-Corson et al., 2009); (c) Leaf wax nC_{29} $\delta^{2}H$ at the Xichagou section (XCG) (this study); (d) Carbonate $\delta^{18}O$ at the Huatugou section (HTG) (Li et al., 2016b); (e) Leaf wax nC_{29} $\delta^{2}H$ at the Hongliugou section (HLG) (this study); (f) Carbonate $\delta^{18}O$ at the Hongliugou (HLG) (Kent-Corson et al., 2009); (g) Carbonate $\delta^{18}O$ at the Dahonggou section (DHG) (Sun et al., 2020); (h) Carbonate $\delta^{18}O$ at the Xiao Qaidam section (XQ) (Kent-Corson et al., 2009); (i) Carbonate $\delta^{18}O$ at the Fenghuangshan section (FHS) (Li et al., 2016a). $\delta^{2}H_{lw}$, leaf wax $\delta^{2}H$. $\delta^{18}O_c$, carbonate $\delta^{18}O$. All isotope data are reported to VSMOW. The black lines represent the results of loess regression (40% smoothing span). The box highlights the interval of expanded lacustrine deposits in the Qaidam Basin. The arrows indicate the variation trend of $\delta^{2}H$ and $\delta^{18}O$. The colors are the same as Fig. 6A. (For interpretation of the colors in the figure(s), the reader is referred to the web version of this article.)

Clues on the impact of temperature variations on climate in Inner Asia can be gained from modern observations. High temperature enhances the static stability of the atmosphere, which would subsequently restrain the air mass subsidence in subtropical zones and shifts subtropical high poleward (Frierson et al., 2007). Under global warming, the subtropical high and westerlies migrate poleward (Frierson et al., 2007); and satellite observations show the poleward displacement of subtropical high with 2-5° due to global warming since 1979 (Johanson and Fu, 2009). We interpret that this global temperature-related mechanism accounts for the co-variation between temperature and hydroclimate histories (Fig. 4). In warm Eocene, generally high temperature and $\delta^{2}H$ suggest a warm and dry climate dominated by subtropical high, which is reflected by xerophytic pollens and evaporite minerals in Guo et al. (2008). In the Oligocene icehouse and the short cooling interval during 38-36 Ma, the cool temperature causes the equatorward shift of subtropical high. The westerlies sequentially dominate the previous subtropical high areas, bringing moisture to Inner Asia and causing a wetter climate with expanded paleo-lake and low leaf wax $\delta^{2}H$. Short intervals of warming and relatively high $\delta^{2}H$ in the Oligocene may indicate the transient weakening influence or deflection of westerlies from Inner Asia.

The East Asian summer monsoon may have been present since the Eocene (Licht et al., 2014). Hence the global cooling driven-migration of subtropical high and westerlies was likely constrained in Inner Asia beyond the influence of the East Asian summer monsoon. We acknowledge that the uncertainties exist regarding the presence and evolution of East Asian monsoon and the paleoecology in Inner Asia, which might confound the global temperature-driven mechanism in our interpretations. For example, a recent study notes the steppe-desert biome in Central Asia (Barbolini et al., 2020) in contrast to the wetter environment in the Qaidam Basin suggested by the fossils of fish and broad-leaved trees (Song et al., 2020; Wang et al., 2007). Also, recent numerical modelings (e.g., Tardif et al., 2020) suggest the absence of East Asian monsoon in the Eocene rather than the presence of the modern-like monsoon in this greenhouse period (Licht et al., 2014). We highlight that the inconsistencies call for a holistic collaboration for understanding the interactions between paleohydrology, paleoecology, and numerical modeling.

After ca. 24 Ma, leaf wax $\delta^{2}H$ becomes higher at the Hongliugou section, and the high values continue during the early-middle Miocene (Fig. 4A). This trend is consistent with the generally increasing $\delta^{18}O$ of fluvial-lacustrine carbonate in Neogene across western Inner Asia, including the Tarim and Qaidam Basin (Kent-Corson et al., 2009). The increase in our $\delta^{2}H$ is coeval with the latest Oligocene-early Miocene warming and occurs in the interval of the regression from lacustrine facies to fluvial-deltaic facies (Fig. 5). The increasing temperature would impart high $\delta^{2}H$ values to precipitation, which are eventually recorded by the leaf wax

δ^2H. High temperature may also have driven the expansion of subtropical high over the Qaidam Basin and cause aridification, which enriches the heavy isotopes of hydrogen. The increase of δ^2H at the Xichagou section is less prominent and the magnitude is smaller than that at the Hongliugou section (Fig. 4A). The difference may reflect the impact of the local sedimentary environment. In the early Miocene, the Xichagou region was close to the depocenter of Qaidam Basin and was dominated by the lacustrine environment (Li et al., 2016b), which might counteract the impact of aridification with local moistures. Besides the sedimentary environment, the uplift of Altun Shan (Yin et al., 2002) likely increased inputs of lipid wax from higher elevations, which caused the relatively lower δ^2H via isotopic fractionation during precipitation processes (Araguas-Araguas et al., 1996).

6. Conclusions

To resolve the contradiction between the Oligocene lacustrine expansion in Qaidam Basin and the aridification in Inner Asia, we reconstructed a long-term (ca. 51 to 12 Ma) paleohydrological record using leaf wax *n*-alkane δ^2H. Our results show a large increase (23.9‰) of δ^2H in the late Eocene, which supports the aridification due to the retreat of the Paratethys Sea. High δ^2H values remain until ca. 34 Ma when the δ^2H decreases sharply at the EOT. In Oligocene, δ^2H values are low and variable, which are accompanied by dominant lacustrine sediments with deltaic intercalations, suggesting a generally wet and variable climate. Our δ^2H results are consistent with the regional carbonate δ^{18}O studies in the westerlies region, which suggest a wetter climate in western Inner Asia during the Oligocene. However, carbonate δ^{18}O studies from monsoon-dominating Inner Asia record a drying trend since the EOT. This contrasting pattern indicates that climates are driven by different mechanisms in the westerlies and monsoon regions. Wetting in Inner Asia is driven by the shift of the climate regime from subtropical high to westerlies that transport more moisture. The aridification of monsoon-dominating areas is linked to the weakened East Asian summer monsoon in response to global cooling. In the early Miocene, global warming restored the arid climate, which led to the shrink of the Qaidam paleo-lake. Given the complexity of the Inner Asia climate revealed in previous studies, further climate proxy studies and numerical modelings are needed to test the response of subtropical high and westerlies to global temperature.

CRediT authorship contribution statement

Minghao Wu: Conceptualization, Formal analysis, Investigation, Methodology, Writing – original draft. **GuangSheng Zhuang:** Conceptualization, Funding acquisition, Methodology, Supervision, Writing – review & editing. **Mingqiu Hou:** Investigation. **Zhonghui Liu:** Writing – review & editing.

Declaration of competing interest

The authors declare that they have no known competing financial interests or personal relationships that could have appeared to influence the work reported in this paper.

Acknowledgements

We would like to thank Editor Rebecca Bendick and two reviewers for their constructive comments that greatly improve the quality of the paper. This work is supported by U.S. National Science Foundation Grant (EAR-2022282) to G. Zhuang.

Appendix A. Supplementary material

Supplementary material related to this article can be found online at https://doi.org/10.1016/j.epsl.2021.116935.

References

An, Z., 2000. The history and variability of the East Asian paleomonsoon climate. Quat. Sci. Rev. 19, 171–187.
Araguas-Araguas, L., Danesi, P., Froehlich, K., Rozanski, K., 1996. Global monitoring of the isotopic composition of precipitation. J. Radioanal. Nucl. Chem. 205, 189–200.
Barbolini, N., Woutersen, A., Dupont-Nivet, G., Silvestro, D., Tardif, D., Coster, P.M.C., Meijer, N., Chang, C., Zhang, H.X., Licht, A., Rydin, C., Koutsodendris, A., Han, F., Rohrmann, A., Liu, X.J., Zhang, Y., Donnadieu, Y., Fluteau, F., Ladant, J.B., Le Hir, G., Hoorn, C., 2020. Cenozoic evolution of the steppe-desert biome in Central Asia. Sci. Adv. 6 (41), eabb8227.
Bosboom, R., Dupont-Nivet, G., Grothe, A., Brinkhuis, H., Villa, G., Mandic, O., Stoica, M., Kouwenhoven, T., Huang, W., Yang, W., Guo, Z., 2014a. Timing, cause and impact of the late Eocene stepwise sea retreat from the Tarim Basin (west China). Palaeogeogr. Palaeoclimatol. Palaeoecol. 403, 101–118.
Bosboom, R.E., Abels, H.A., Hoorn, C., van den Berg, B.C.J., Guo, Z., Dupont-Nivet, G., 2014b. Aridification in continental Asia after the Middle Eocene Climatic Optimum (MECO). Earth Planet. Sci. Lett. 389, 34–42.
Broccoli, A.J., Manabe, S., 1992. The effects of orography on midlatitude northern hemisphere dry climates. J. Climate 5, 1181–1201.
Bush, M.A., Saylor, J.E., Horton, B.K., Nie, J., 2016. Growth of the Qaidam Basin during Cenozoic exhumation in the northern Tibetan Plateau: inferences from depositional patterns and multiproxy detrital provenance signatures. Lithosphere 8, 58–82.
Carroll, A.R., Bohacs, K.M., 1999. Stratigraphic classification of ancient lakes: balancing tectonic and climatic controls. Geology 27 (2), 99–102.
Caves, J.K., Winnick, M.J., Graham, S.A., Sjostrom, D.J., Mulch, A., Chamberlain, C.P., 2015. Role of the westerlies in Central Asia climate over the Cenozoic. Earth Planet. Sci. Lett. 428, 33–43.
Chang, H., Li, L., Qiang, X., Garzione, C.N., Pullen, A., An, Z., 2015. Magnetostratigraphy of Cenozoic deposits in the western Qaidam Basin and its implication for the surface uplift of the northeastern margin of the Tibetan Plateau. Earth Planet. Sci. Lett. 430, 271–283.
Chen, F., Chen, J., Huang, W., Chen, S., Huang, X., Jin, L., Jia, J., Zhang, X., An, C., Zhang, J., Zhao, Y., Yu, Z., Zhang, R., Liu, J., Zhou, A., Feng, S., 2019. Westerlies Asia and monsoonal Asia: spatiotemporal differences in climate change and possible mechanisms on decadal to sub-orbital timescales. Earth-Sci. Rev. 192, 337–354.
Cheng, F., Garzione, C., Jolivet, M., Guo, Z., Zhang, D., Zhang, C., 2018. A new sediment accumulation model of Cenozoic depositional ages from the Qaidam Basin, Tibetan Plateau. J. Geophys. Res., Earth Surf. 123, 3101–3121.
Deaton, B.C., Balsam, W.L., 1991. Visible spectroscopy – a rapid method for determining hematite and goethite concentration in geological materials. J. Sediment. Res. 61, 628–632.
Du, Q., Sun, S., 1990. Vegetation in the Qaidam Basin Region and Its Utilization. Science Press, Beijing, p. 6 (in Chinese with English title).
Dupont-Nivet, G., Krijgsman, W., Langereis, C.G., Abels, H.A., Dai, S., Fang, X., 2007. Tibetan Plateau aridification linked to global cooling at the Eocene-Oligocene transition. Nature 445, 635–638.
Fan, M.J., Ayyash, S.A., Tripati, A., Passey, B.H., Griffith, E.M., 2018. Terrestrial cooling and changes in hydroclimate in the continental interior of the United States across the Eocene-Oligocene boundary. Geol. Soc. Am. Bull. 130, 1073–1084.
Fang, X., Zhang, W., Meng, Q., Gao, J., Wang, X., King, J., Song, C., Dai, S., Miao, Y., 2007. High-resolution magnetostratigraphy of the Neogene Huaitoutala section in the eastern Qaidam Basin on the NE Tibetan Plateau, Qinghai Province, China and its implication on tectonic uplift of the NE Tibetan Plateau. Earth Planet. Sci. Lett. 258, 293–306.
Frierson, D.M.W., Lu, J., Chen, G., 2007. Width of the Hadley cell in simple and comprehensive general circulation models. Geophys. Res. Lett. 34 (18), L18804.
Graham, S.A., Chamberlain, C.P., Yue, Y., Ritts, B.D., Hanson, A.D., Horton, T.W., Waldbauer, J.R., Poage, M.A., Feng, X., 2005. Stable isotope records of Cenozoic climate and topography, Tibetan Plateau and Tarim basin. Am. J. Sci. 305, 101–118.
Guo, Z.T., Sun, B., Zhang, Z.S., Peng, S.Z., Xiao, G.Q., Ge, J.Y., Hao, Q.Z., Qiao, Y.S., Liang, M.Y., Liu, J.F., Yin, Q.Z., Wei, J.J., 2008. A major reorganization of Asian climate by the early Miocene. Clim. Past 4, 153–174.
Han, W., 2008. Climatic records of Cenozoic sediments from Qaidam Basin and their implications on drying of Asian Inland. Doctor Dissertation. Lanzhou: Lanzhou University.
Hren, M.T., Sheldon, N.D., Grimes, S.T., Collinson, M.E., Hooker, J.J., Bugler, M., Lohmann, K.C., 2013. Terrestrial cooling in Northern Europe during the eocene-oligocene transition. Proc. Natl. Acad. Sci. USA 110, 7562–7567.
Johanson, C.M., Fu, Q., 2009. Hadley cell widening: model simulations versus observations. J. Climate 22, 2713–2725.

Kent-Corson, M.L., Ritts, B.D., Zhuang, G., Bovet, P.M., Graham, S.A., Chamberlain, C.P., 2009. Stable isotopic constraints on the tectonic, topographic, and climatic evolution of the northern margin of the Tibetan Plateau. Earth Planet. Sci. Lett. 282, 158–166.

Lai, J., Fan, X., Pang, X., Zhang, X., Xiao, C., Zhao, X., Han, C., Wang, G., Qin, Z., 2019. Correlating diagenetic facies with well logs (conventional and image) in sandstones: the Eocene–Oligocene Suweiyi Formation in Dina 2 Gasfield, Kuqa depression of China. J. Pet. Sci. Eng. 174, 617–636.

Li, B., Sun, D., Wang, X., Zhang, Y., Hu, W., Wang, F., Li, Z., Ma, Z., Liang, B., 2016a. $\delta^{18}O$ and $\delta^{13}C$ records from a Cenozoic sedimentary sequence in the Lanzhou Basin, Northwestern China: implications for palaeoenvironmental and palaeoecological changes. J. Asian Earth Sci. 125, 22–36.

Li, B., Yan, M., Zhang, W., Parés, J.M., Fang, X., Yang, Y., Zhang, D., Guan, C., Bao, J., 2020. Magnetic fabric constraints on the Cenozoic compressional strain changes in the northern Qaidam marginal thrust belt and their tectonic implications. Tectonics 39 (6), e2019TC005989.

Li, L., Garzione, C.N., 2017. Spatial distribution and controlling factors of stable isotopes in meteoric waters on the Tibetan Plateau: implications for paleoelevation reconstruction. Earth Planet. Sci. Lett. 460, 302–314.

Li, L., Garzione, C.N., Pullen, A., Chang, H., 2016b. Early-middle Miocene topographic growth of the northern Tibetan Plateau: stable isotope and sedimentation evidence from the southwestern Qaidam basin. Palaeogeogr. Palaeoclimatol. Palaeoecol. 461, 201–213.

Li, Q., Zhang, Y., Dong, L., Guo, Z., 2018. Oligocene syndepositional lacustrine dolomite: a study from the southern Junggar Basin, NW China. Palaeogeogr. Palaeoclimatol. Palaeoecol. 503, 69–80.

Licht, A., van Cappelle, M., Abels, H.A., Ladant, J.B., Trabucho-Alexandre, J., France-Lanord, C., Donnadieu, Y., Vandenberghe, J., Rigaudier, T., Lecuyer, C., Terry, D., Adriaens Jr., R., Boura, A., Guo, Z., Soe, A.N., Quade, J., Dupont-Nivet, G., Jaeger, J.J., 2014. Asian monsoons in a late Eocene greenhouse world. Nature 513, 501–506.

Liu, Z., He, Y., Jiang, Y., Wang, H., Liu, W., Bohaty, S.M., Wilson, P.A., 2018. Transient temperature asymmetry between hemispheres in the Palaeogene Atlantic Ocean. Nat. Geosci. 11, 656–660.

Meijer, N., Dupont-Nivet, G., Abels, H.A., Kaya, M.Y., Licht, A., Xiao, M., Zhang, Y., Roperch, P., Poujol, M., Lai, Z., Guo, Z., 2019. Central Asian moisture modulated by proto-Paratethys Sea incursions since the early Eocene. Earth Planet. Sci. Lett. 510, 73–84.

Nie, J., Ren, X., Saylor, J.E., Su, Q., Horton, B.K., Bush, M.A., Chen, W., Pfaff, K., 2019. Magnetic polarity stratigraphy, provenance, and paleoclimate analysis of Cenozoic strata in the Qaidam Basin, NE Tibetan Plateau. GSA Bull. 132 (1–2), 310–320.

Page, M., Licht, A., Dupont-Nivet, G., Meijer, N., Barbolini, N., Hoorn, C., Schauer, A., Huntington, K., Bajnai, D., Fiebig, J., Mulch, A., Guo, Z., 2019. Synchronous cooling and decline in monsoonal rainfall in northeastern Tibet during the fall into the Oligocene icehouse. Geology 47 (3), 203–206.

Sachse, D., Billault, I., Bowen, G.J., Chikaraishi, Y., Dawson, T.E., Feakins, S.J., Freeman, K.H., Magill, C.R., McInerney, F.A., van der Meer, M.T.J., Polissar, P., Robins, R.J., Sachs, J.P., Schmidt, H.L., Sessions, A.L., White, J.W.C., West, J.B., Kahmen, A., 2012. Molecular paleohydrology: interpreting the hydrogen-isotopic composition of lipid biomarkers from photosynthesizing organisms. Annu. Rev. Earth Planet. Sci. 40, 221–249.

Shao, L., Stattegger, K., Li, W., Haupt, B.J., 1999. Depositional style and subsidence history of the Turpan Basin (NW China). Sediment. Geol. 128, 155–169.

Song, B., Spicer, R.A., Zhang, K., Ji, J., Farnsworth, A., Hughes, A.C., Yang, Y., Han, F., Xu, Y., Spicer, T., Shen, T., Lunt, D.J., Shi, G., 2020. Qaidam Basin leaf fossils show northeastern Tibet was high, wet and cool in the early Oligocene. Earth Planet. Sci. Lett. 537, 116175.

Sun, Y., Liu, J., Liang, Y., Ji, J., Liu, W., Aitchison, J.C., Sun, J., Lu, J., Song, B., Xu, Y., Zhang, K., Liu, Z., 2020. Cenozoic moisture fluctuations on the northeastern Tibetan Plateau and association with global climatic conditions. J. Asian Earth Sci. 200, 104490.

Sun, Z.M., Yang, Z.Y., Pei, J.L., Ge, X.H., Wang, X.S., Yang, T.S., Li, W.M., Yuan, S.H., 2005. Magnetostratigraphy of Paleogene sediments from northern Qaidam Basin, China: implications for tectonic uplift and block rotation in northern Tibetan Plateau. Earth Planet. Sci. Lett. 237, 635–646.

Tardif, D., Fluteau, F., Donnadieu, Y., Le Hir, G., Ladant, J.-B., Sepulchre, P., Licht, A., Poblete, F., Dupont-Nivet, G., 2020. The origin of Asian monsoons: a modelling perspective. Clim. Past 16, 847–865.

Wang, W., Zheng, W., Zhang, P., Li, Q., Kirby, E., Yuan, D., Zheng, D., Liu, C., Wang, Z., Zhang, H., Pang, J., 2017. Expansion of the Tibetan Plateau during the Neogene. Nat. Commun. 8, 15887.

Wang, X.M., Qiu, Z.D., Li, Q., Wang, B.Y., Qiu, Z.X., Downs, W.R., Xie, G.P., Xie, J.Y., Deng, T., Takeuchi, G.T., Tseng, Z.J., Chang, M.M., Liu, J., Wang, Y., Biasatti, D., Sun, Z.C., Fang, X.M., Meng, Q.Q., 2007. Vertebrate paleontology, biostratigraphy, geochronology, and paleoenvironment of Qaidam Basin in northern Tibetan Plateau. Palaeogeogr. Palaeoclimatol. Palaeoecol. 254, 363–385.

Yin, A., Rumelhart, P.E., Butler, R., Cowgill, E., Harrison, T.M., Foster, D.A., Ingersoll, R.V., Qing, Z., Xian-Qiang, Z., Xiao-Feng, W., Hanson, A., Raza, A., 2002. Tectonic history of the Altyn Tagh fault system in northern Tibet inferred from Cenozoic sedimentation. Geol. Soc. Am. Bull. 114, 1257–1295.

Yin, A., Dang, Y., Zhang, M., Chen, X., McRivette, M.W., 2008. Cenozoic tectonic evolution of the Qaidam basin and its surrounding regions (part 3): structural geology, sedimentation, and regional tectonic reconstruction. Geol. Soc. Am. Bull. 120, 847–876.

Yue, Y., Ritts, B.D., Graham, S.A., Wooden, J.L., Gehrels, G.E., Zhang, Z., 2003. Slowing extrusion tectonics: lowered estimate of post-Early Miocene slip rate for the Altyn Tagh fault. Earth Planet. Sci. Lett. 217, 111–122.

Zachos, J., Pagani, M., Sloan, L., Thomas, E., Billups, K., 2001. Trends, rhythms, and aberrations in global climate 65 Ma to present. Science 292, 686–693.

Zhang, W., 2006. Cenozoic Uplift of the Tibetan Plateau: Evidence from High Resolution Magnetostratigraphy of the Qaidam Basin. Lanzhou University, Lanzhou.

Zhang, Z., Wang, H., Guo, Z., Jiang, D., 2007. What triggers the transition of palaeoenvironmental patterns in China, the Tibetan Plateau uplift or the Paratethys Sea retreat? Palaeogeogr. Palaeoclimatol. Palaeoecol. 245, 317–331.

Zhuang, G., Hourigan, J.K., Ritts, B.D., Kent-Corson, M.L., 2011. Cenozoic multiple-phase tectonic evolution of the northern Tibetan Plateau: constraints from sedimentary records from Qaidam Basin, Hexi Corridor, and Subei Basin, northwest China. Am. J. Sci. 311 (2), 116–152.